Available online at www.sciencedirect.com

ScienceDirect

Advances in Space Research 73 (2024) 4393–4413

ADVANCES IN SPACE RESEARCH (a COSPAR publication)

www.elsevier.com/locate/asr

Particle-In-Cell simulation of electrostatic waves in the ionosphere

Rakesh Moulick [a,b], Sayan Adhikari [c,d], Gunjan Sharma [a], B.K. Saikia [a,b], W.J. Miloch [c,*]

[a] Centre of Plasma Physics, Institute for Plasma Research, Nazirakhat, Kamrup(M), Assam, Sonapur, 782402, India
[b] Homi Bhaba National Institute, Training School Complex, Anushaktinagar, Mumbai, 400094, India
[c] Department of Physics, University of Oslo, Blindern, 0316, Oslo, Norway
[d] Institute for Energy Technology, Instituttveien 8, 2007, Kjeller, Norway

Received 8 August 2023; received in revised form 11 January 2024; accepted 7 February 2024
Available online 12 February 2024

Abstract

In the upper atmosphere (ionosphere), plasma with two electron populations is very common. The cold electrons ($T_e \sim 1$ eV) usually originate in the ionosphere, while the hot electrons ($T_e \sim 100$ eV) come from the magnetosphere. In addition to these two electron populations, there may be a beam of electrons streaming along the magnetic field lines. These electrons are responsible for exciting various electrostatic wave modes. In this article, we provide a systematic insight in the evolution of the system, based on the beam energy. With an increase in beam velocity, the beam temporarily recovers a portion of its initial energy as well as a higher saturation energy. The wave energy is lost significantly before saturation and after linear growth at a relatively modest beam velocity. In addition, the low beam velocity generates BGK electron holes in the phase space, which are missing at higher beam velocities. We also present the analysis of the condition of sustained electron holes in the phasespace.

Keywords: 82D10; 74A25; 82B40; 76E20

1. Introduction

The Sun's magnetic activity changes periodically (∼ 11 years) leading to varying occurences of phenomena such as solar flares and coronal mass ejections (Karak et al. 2018). The coronal mass brings with it a stream of highly energetic particles. The solar material confined by the coronal magnetic field is ejected outwards into the space at a speed of about 270 km/sec (Parks 2019). The Earth's magnetosphere restricts majority of the incoming particles from entering into the Earth's atmosphere. Besides, the solar ultraviolet radiation ionizes a portion of the Earth's neutral atmosphere, and due to infrequent collisions resulting in slow recombination, a permanent ionized atmosphere is formed, which is known as the ionosphere. The Earth has its ionosphere beginning at around 60 km from the surface and extending up into the magnetosphere, which starts at around 500 km above the Earth's surface (Cowley 2007). Binary collisions, which are common in most of the laboratory plasmas, are rare in the ionospheric plasmas and such plasma is normally considered as collisionless (Parks 2019). However, it should be noted that collisions do occur to a greater extent in the lower E-region of the ionosphere (Brask et al. 2022). Ionosphere is the home to many satellites. Being a layer for the satellite signals, change in the ionospheric conditions have influence on the electromagnetic waves used for navigation and communications (Sharifi and Farzaneh 2016; Langley 2000).

The study of the plasma environments in the upper atmosphere of planets, particularly those of the Earth, Mars, and the Jovian planets, has gained wide popularity in recent times (Garrett et al. 2016; Russell 2010). The knowledge of the electrodynamics phenomena happening

* Corresponding author.
E-mail address: w.j.miloch@fys.uio.no (W.J. Miloch).

https://doi.org/10.1016/j.asr.2024.02.009
0273-1177/

in the Earth's upper atmosphere exemplifies similar dynamics in other planetary systems. The Earth's ionosphere is responsible for many electrostatic phenomena such as the Broadband Electrostatic Noise (BEN). BEN are the high and low frequency electrostatic fluctuations (Singh et al. 2009; Mbuli et al. 2018). The exact cause and effect of the phenomena is debatable, albeit, the magnetic field aligned electron beams along with a coexisting source of hot and cold electrons may explain the BEN (Lu et al. 2005; Singh et al. 2009; Lin et al. 1984; Tokar and Gary 1984). The cold electrons usually originate in the ionosphere, while the hot electrons often come from the magnetosphere. The beam electrons act as the free energy sources that trigger the streaming instabilities (Bohm and Gross 1949). In a laboratory plasma, BEN has been experimentally achieved by compressing a magnetized plasma (DuBois et al. 2014). Laboratory scale methods of controlled production of two electron-temperature plasma has been emphasized in Sharma et al. (2022).

There are many works that discuss the phase space hole and bipolar electric field structures appearing in the ionosphere especially on the basis of the FAST satellite observations (Goldman et al. 2000; Crary et al. 2001; Newman et al. 2001). The evidence of presence of hot and cold electrons have been presented in Pottelette et al. (1999). The bipolar electric field structures are associated with the two-stream instabilities and appear when the instability saturates. The non-linear evolution of such instabilities gives rise to the phase space holes.

A good insight into the physics of beam-plasma interactions can be manifested via particle simulations. Some of the recent studies have been portrayed in Norgren et al. (2022); Sun et al. (2022); Schamel (2023). Kinetic studies enable us to explore the enriching physics of beam-plasma systems that are relevant to the ionospheric environment. For example, Dum (1990) had shown, for a relatively colder beam, primarily, the beam mode is excited with a growth rate slightly below the plasma frequency. A transition from reactive to kinetic instability is caused by the broadening of the beam, where the drift energy of the beam is gradually lost to the electric field. This, in turn, excites wave modes of larger wave numbers. Since various oscillatory modes can be present in a beam-plasma system, the wave-wave interaction processes also have a vital role to play. A forward propagating beam-excited Langmuir wave can merge with an existing ion acoustic mode and consequently generate a backward propagating ion-acoustic wave (Kasaba et al. 2001). This process is responsible for the transfer of energy from one Langmuir wave to another via wave-wave coupling and is thought to be the initial step of type III radio emission (Ginzburg and Zhelezniakov 1958). In a Vlasov-Poisson simulation of the solar wind, Henri et al. (2010) have shown that the electrostatic decay of beam-driven Langmuir waves is possible when the ion temperature is close to the electron temperature. Such energy transfer processes from one mode/species to another are key to many physical observations. In this regard, an important finding has been reported by An et al. (2017). In a PIC simulation study, they have shown that in the presence of a magnetic field, for a gyrating field-aligned electron beam, the energy transfer rate is faster between the electron beam and electrostatic waves, resulting in the suppression of the whistler instability by the electrostatic instability. Furthermore, Chakrabarti and Sengupta (2009) have highlighted the nonlinear interaction of the electron acoustic and electron plasma waves. Vlasov-Poisson simulation of two temperature electrons exhibiting the formation of Double Layers and holes have been explored in Saharia and Goswami (2007); Saharia and Goswami (2008) for the first time.

Though the system of hot and cold electrons in the presence of a beam has been previously addressed (Lu et al. 2005; Koen et al. 2012), yet there are some open questions. The effect of beam velocity on the kinetic energy profile, saturation of the instability, conditional analysis of the instability along with the condition for sustained electrostatic solitary wave has not been widely discussed especially in the context of Particle-In-Cell simulation. To address the open questions, in this paper, we specifically attempt to highlight such issues including the effect of hot to cold electron density ratio as well as the temperature. We have chosen the Particle-In-Cell technique for the investigation. Furthermore, the distribution of energies among the individual species has been discussed in details. Along with this, we examine each phase space, highlighting the creation of holes in the beam phase space and commenting about the corresponding correlation on the hot electron phase space. Despite the fact that the subject has been explored by many academics, using many different methods, there are still some obscure regions of scientific interest. This paper is an attempt to address some of those and the results are believed to progressively add new information to this field.

In the following, section II deals with the simulation model, section III deals with the results, and finally, the paper has been concluded in section IV.

2. Simulation Model

There are three populations of electrons in the model. Ions being massive and non-responsive to the fast oscillating electric fields of electrons, are considered to form a neutral background. The total unperturbed electron density is $n_{e0} = n_{c0} + n_{h0} + n_{b0}$ where, n_{c0}, n_{h0} and n_{b0} denote the unperturbed density of the cold, hot and beam electrons respectively. The plasma frequency of the j^{th} electron population (species) is written as

$$\omega_{pj} = \left(\frac{n_{j0}e^2}{m_e\epsilon_0}\right)^{\frac{1}{2}} \tag{1}$$

Here, n_{j0} stands for the density of the j^{th} electron species, e is the electric charge, ϵ_0 is the permittivity of free space and

m_e is the mass of an electron. The Debye length of the j^{th} species is given by:

$$\lambda_{Dj} = \left(\frac{\epsilon_0 T_j}{n_{j0} e^2}\right)^{\frac{1}{2}} \tag{2}$$

Here, T_j stands for the temperature of the j^{th} species in units of energy (Joules). The analytical expressions for the dispersion relations corresponding to the electron acoustic wave, electron plasma wave, and electron beam wave, respectively are given by Koen et al. (2012)

$$\omega^2 = \omega_{pc}^2 \left(\frac{1 + 3k^2\lambda_{Dc}^2}{1 + 1/k^2\lambda_{Dh}^2}\right) \tag{3}$$

$$\omega^2 = \omega_{pc}^2 \left(1 + 3k^2\lambda_{Dc}^2\right) + \omega_{ph}^2 \left(1 + 3k^2\lambda_{Dh}^2\right) \tag{4}$$

$$\omega = \frac{k u_d}{1 + n_b/n_{e0}} \approx k u_d \tag{5}$$

Here, k is the magnitude of the one-dimensional wave vector and u_d is the beam speed. $\omega_{pc,h}$ and $\lambda_{Dc,h}$ represents the plasma frequency and Debye length of the cold and the hot species respectively. The Particle-In-Cell code "SPIC (PIC for Space Plasmas)[1]" has been developed to study the system under consideration. SPIC is a one-dimensional electrostatic code with periodic boundary conditions. The creation of one's own code is thought to offer more implementation control and flexibility. The code can be expanded to implement any further requirement. The code considers the electrons and ions as simulation particles, and initial velocity distribution has been sampled out of a Maxwellian distribution for all the species. However, the beam electrons have a streaming velocity, in addition to their Maxwellian component. The system under consideration is collisionless with no ambient magnetic field. The code has been fully normalized with the following normalization scheme.

$t' = \omega_{pe} t$, where $\omega_{pe} = \sqrt{n_{e0} e^2/\epsilon_0 m_e}$ is the total electron plasma frequency and t is time

$x' = x/\lambda_D$ where, λ_D is the characteristic Debye length corresponding to the temperature of the cold electrons (T_{ec}) and the total equilibrium electron density n_{e0}. Thus,

$$\lambda_D = \left(\frac{\epsilon_0 T_{ec}}{n_{e0} e^2}\right)^{\frac{1}{2}} \tag{6}$$

$v' = v/v_{Tc} = v/(\omega_{pc}\lambda_{Dc})$ where, v_{Tc} is the thermal velocity of the cold electron species.

$\phi' = e\phi/T_{ec}$ where, T_{ec} is the cold electron temperature and

$E' = \left(\frac{e}{m_e \omega_{pe}^2 \lambda_D}\right) E$

The governing equations of the system (to be simulated via Particle-In-Cell), thus, become:

$$\frac{d^2\phi'}{dx'^2} = -(N_i - N_{ec} - N_{eh} - N_{eb}) \tag{7}$$

$$E' = -\left(\frac{T_{ec}}{m_e \omega_{pe}^2 \lambda_D^2}\right) \frac{d\phi'}{dx'} \tag{8}$$

$$v' = \left(\frac{q}{m}\right)\left(\frac{T_{ec}}{e}\right)\left(\frac{1}{\omega_{pe}\omega_{pc}\lambda_D\lambda_{Dc}}\right) E' t' \tag{9}$$

$$x = \left(\frac{\omega_{pc}}{\omega_{pe}}\right)\left(\frac{\lambda_{Dc}}{\lambda_D}\right) v' t' \tag{10}$$

2.1. Simulation Setup

We consider a one-dimensional simulation domain that has been divided into 1024 cells, the size of each cell being equal to λ_D. The cell spacing in the normalized unit stands for unity. The time step has been considered as $0.01\omega_{pe}^{-1}$. All densities have been normalized by the cold electron density and velocities are expressed in the units of the thermal velocity of the cold electrons. There are 5 million pseudo-particles launched for each species of electrons and corresponding specific weights have been determined. The initial velocity distribution for all the species of electrons is Maxwellian. In addition, the beam electrons have a streaming speed. The code has been written using the parsing utility "ini-parser", which splits the input variables into an "input.ini" file. Python scripts (can be found in the aforementioned GitHub repository) were used to post-process the data.

2.2. Discretization and Charge Density Calculation

The one-dimensional Poisson's equation is discretized as follows Changmai and Bora (2019); Birdsall and Langdon (2004); Brieda (2019):

$$\frac{\phi_{i-1} - 2\phi_i + \phi_{i+1}}{\Delta x^2} = \frac{\rho_i}{\epsilon_0}$$

The subscript "i" denotes the value of the concerned physical quantity at the middle of the cell. Consequently, the electric field is given as follows:

$$E_i = -\frac{\phi_{i+1} - \phi_i}{\Delta x}$$

The charge density at the grid location is calculated from the particle position using the standard method of scattering.

$$\rho = \sum_{j=1}^{N} q_j n_j$$

Where, q_j and n_j are the charge and number density of the species j.

The Poisson's solver which solves for the plasma potential in the domain has been implemented via direct and Gauss-Seidel methods. However, for fast execution, use of a direct solver is suggested.

[1] https://github.com/rakeshmoulick/SPIC

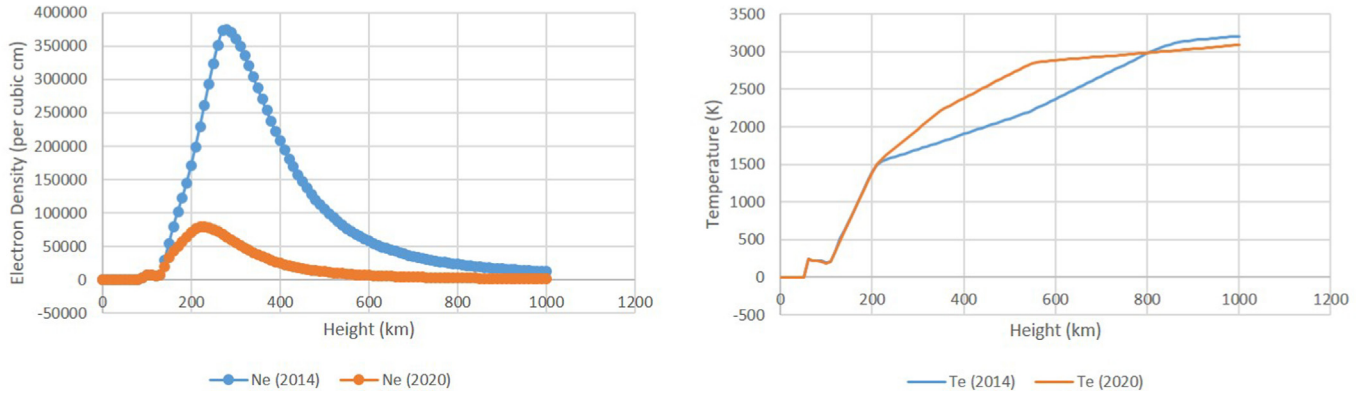

Fig. 1. Plot of the electron density and temperature profiles on 1st Feb. 2014 and 1st Feb. 2020 over Svalbard (77.8750°N, 20.9752°E) at 1 PM using the IRI-2016 model.

3. Results and Discussion

We investigate several distinct cases as shown in Table 1. The results are depicted for a wide range of beam velocities. Additionally, Run-8 to 11 show the variations of electron concentrations as well as temperature. Other parameters are relevant to the upper ionospheric region. It is possible to see that the ionospheric parameters change, depending on the solar activity by comparing the IRI (IRI, 2023) and Solar Progression Cycle (NOAA 2023) data. For example, Fig. 1 shows the electron density and temperature profiles on the 1st Feb. 2014 and 1st Feb. 2020 at 77.8750° N, 20.9752°E (Svalbard) at 1 PM using the IRI-2016 model. This chosen coordinate is reasonably at high latitude and the Earth's magnetic field lines are parallel to the particle flow direction. The observed deviation of the parameters in Fig. 1 is primarily due to the Sun's activity, which is higher in 2014 than it is in 2020. Usually, there are two distinct populations of electrons in the ionosphere (Marif and Lilensten 2020). The first ones are the ambient thermal electrons, whose temperature is on the order of electron volts or less. The second is the population of high energetic electrons having temperature on the order of several kilo electron volts. The high energetic electrons originate due to two main reasons. First, due to the photo-ionization by Extreme Ultra Violet (EUV) radiation, and second, due to Energetic Electron Precipitation (EEP). Originally, the precipitated electrons appear from the solar wind and solar flares. It is important to note that the solar flare electrons are potentially highly energetic, typically, $10-20$ million K in temperature, which, may become as high as 100 million K (Holman and Benedict YYYY). Furthermore, during geomagnetic storms, the magnetosphere and the ionosphere can become strongly coupled and in such a case, the precipitating electrons can reflect back to the magnetosphere. This, in turn, influences the total precipitating flux in the upper ionosphere (about 800 km) (Khazanov et al. 2019).

In this article, the initial cold electron temperature is $T_{ec} = 1eV$ ($\sim 11600K$). Note that a slight variation with the actual data should not disturb the physical aspect of our point of interest. More details on the ionospheric electron temperature are available in Dalgarno et al. (1963). The initial hot electron temperature is $T_{eh} = 100eV$ ($\sim 1160452.5K$). In addition, the system contains beam electrons, which enter the system by following the magnetic field lines. All the three populations of electrons have been sampled out of Maxwellian distribution, following the

Table 1
Simulation parameters for various runs. The background plasma density is $n_0 = 10^{10}m^{-3}$. α stands for the hot to cold electron density ratio and β corresponds to the beam to cold electron density ratio. T_{ec}, T_{eh} and T_{eb} denote the cold, hot and beam electron temperatures. The normalized drift velocity of the beam is denoted by v_d, where, its un-normalized value u_d has been normalized by the cold electron thermal velocity v_{Tec}.

Run	$\alpha = n_{h0}/n_{c0}$	$\beta = n_{b0}/n_{c0}$	$\theta = T_{eh}/T_{ec}$	$\phi = T_{eh}/T_{eb}$	$v_d = u_d/v_{Tc}$
1	1.0	0.04	100.0	100.0	15
2	1.0	0.04	100.0	100.0	20
3	1.0	0.04	100.0	100.0	25
4	1.0	0.04	100.0	100.0	35
5	1.0	0.04	100.0	100.0	40
6	1.0	0.04	100.0	100.0	45
7	1.0	0.04	100.0	100.0	80
8	10.0	0.04	100.0	100.0	40
9	0.1	0.04	100.0	100.0	40
10	1.0	0.04	10.0	10.0	40.0
11	1.0	0.04	50.0	50.0	40.0

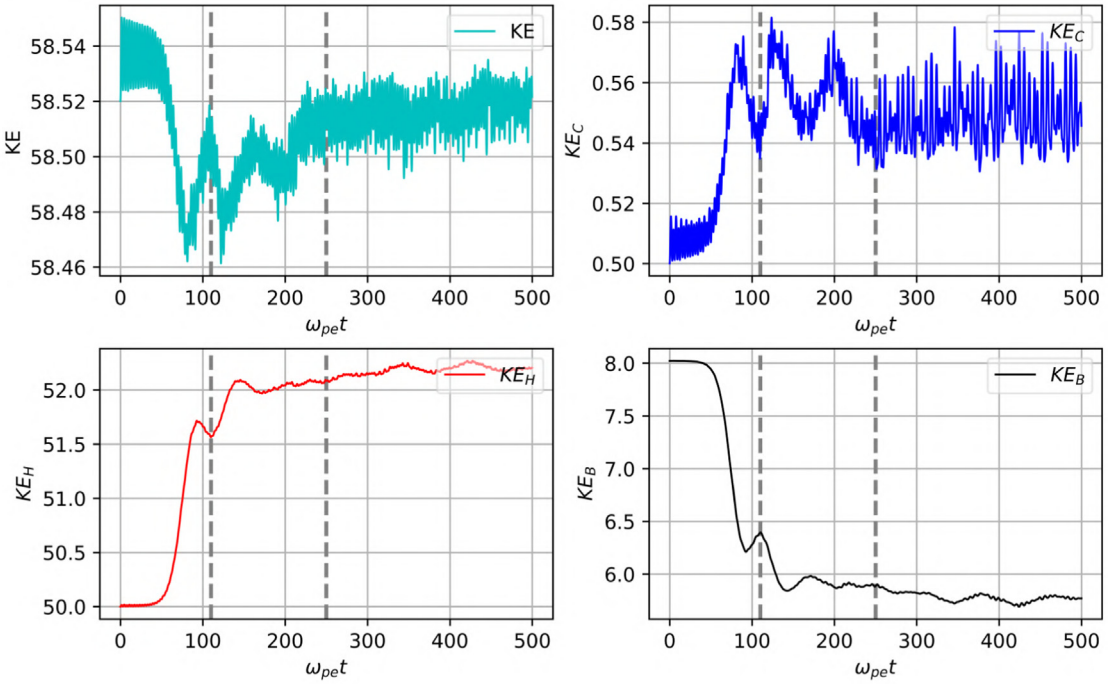

Fig. 2. Plot of the kinetic energy (in normalized units) for $v_d = 20$. While KE denotes the sum total of the kinetic energies of the cold(KE_C), hot(KE_H) and beam(KE_B) electrons respectively. Top left and right plots show the total kinetic energy of the system and kinetic energy of the cold electrons, whereas, the bottom left and right plots show the kinetic energies of the hot and the beam electrons respectively.

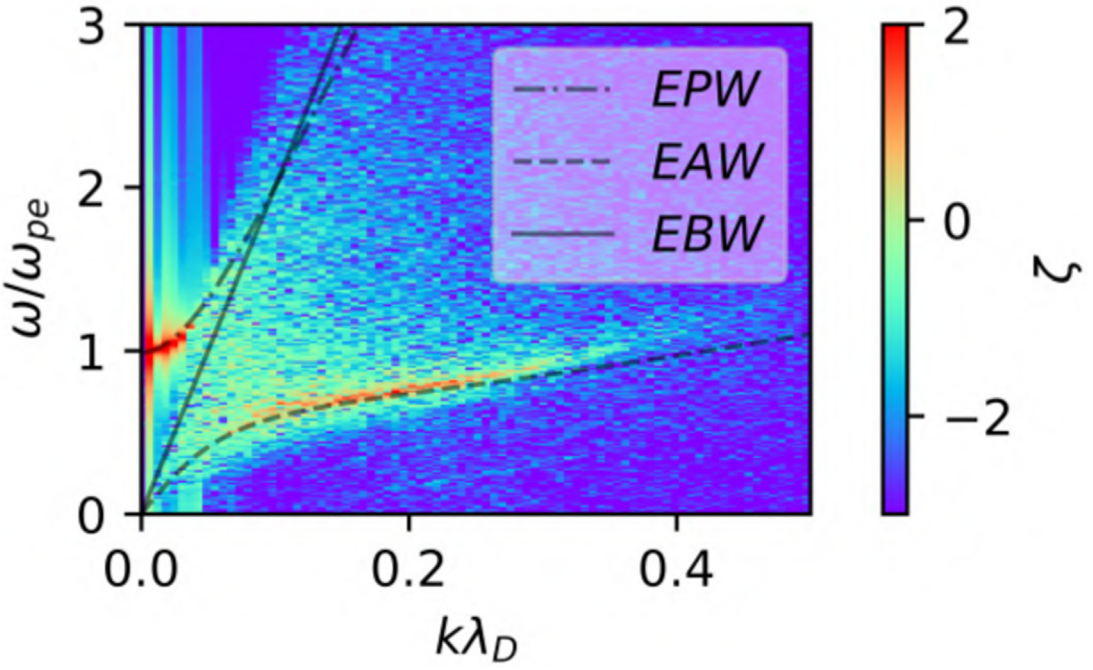

Fig. 3. Dispersion relation for plasma with $v_d = 20$. ζ represents the FFT amplitude of the normalized electric field. *EPW*, *EAW* and *EBW* stands for the electron plasma wave, electron acoustic wave and electron beam wave respectively. The negative values of the FFT amplitude is because of the logarithmic scale of the absolute values of the electric field.

Birdsall's formula (Birdsall and Langdon 2004). The beam is given an initial drift (v_d) in addition to its Maxwellian spread. Thereafter, it is self-consistently maintained following the periodic boundary condition. Periodic boundary has been applied for the other two electron populations as well; however, the ions are at rest. We assume the system to be in a state, such that, the hot and the cold electrons are not in thermal equilibrium with each other. The simulation

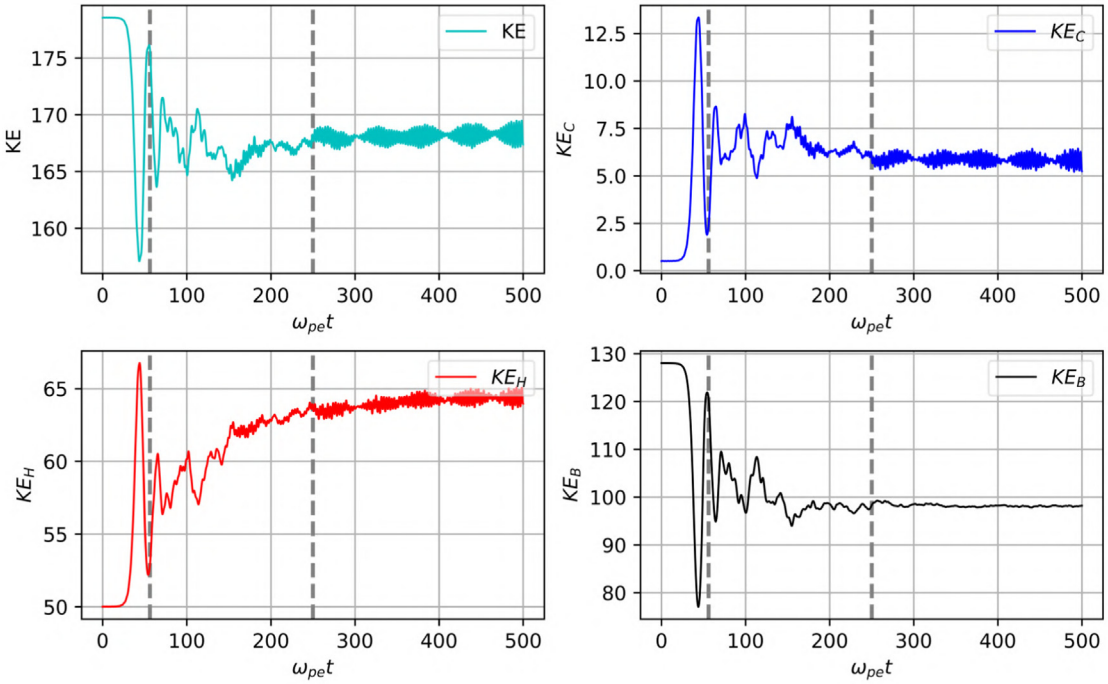

Fig. 4. Plot of the kinetic energy (in normalized units) for $v_d = 80$. Here, KE denotes the total kinetic energy of the system, KE_C, KE_H and KE_B denote the kinetic energies of the cold, hot and beam electrons respectively.

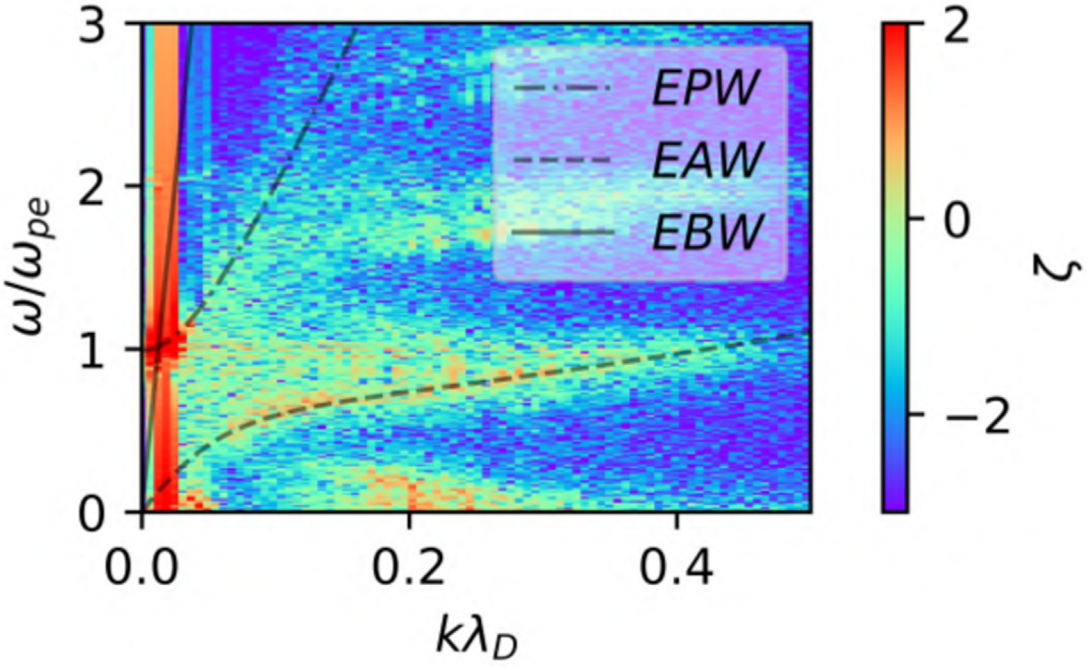

Fig. 5. Dispersion relation of the plasma with $v_d = 80$. ζ represents the FFT amplitude of the normalized electric field.

parameters have been highlighted in Table-1. The explicit values of the relevant physical parameters are: $\lambda_{Dc} = 0.106m, \lambda_{Dh} = 1.06m, \lambda_D = 0.07m, \omega_{pc} = 3.94 \times 10^6 Hz, \omega_{ph} = 3.94 \times 10^6 Hz$, and $\omega_{pe} = 5.64 \times 10^6 Hz, T_{ec} = 1eV, T_{eh} = 100eV$ and $T_{eb} = 1eV$

Fig. 2 shows the kinetic energy at different time instances for the case with a low energy beam ($v_d = 20$, where, $v_d = u_d/v_{Tc}$). The plot shows the drainage of kinetic energy from the beam (KE_B) to the hot and cold electron populations respectively. While the kinetic energies of the

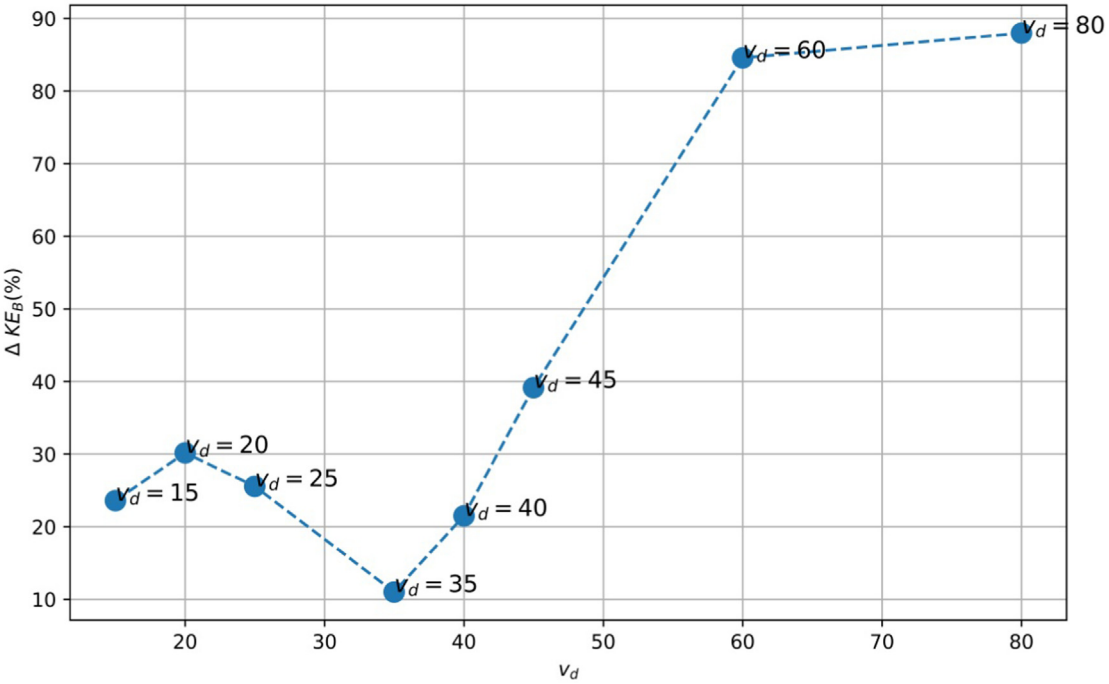

Fig. 6. Percentage of the beam kinetic energy retrieval at different values of v_d.

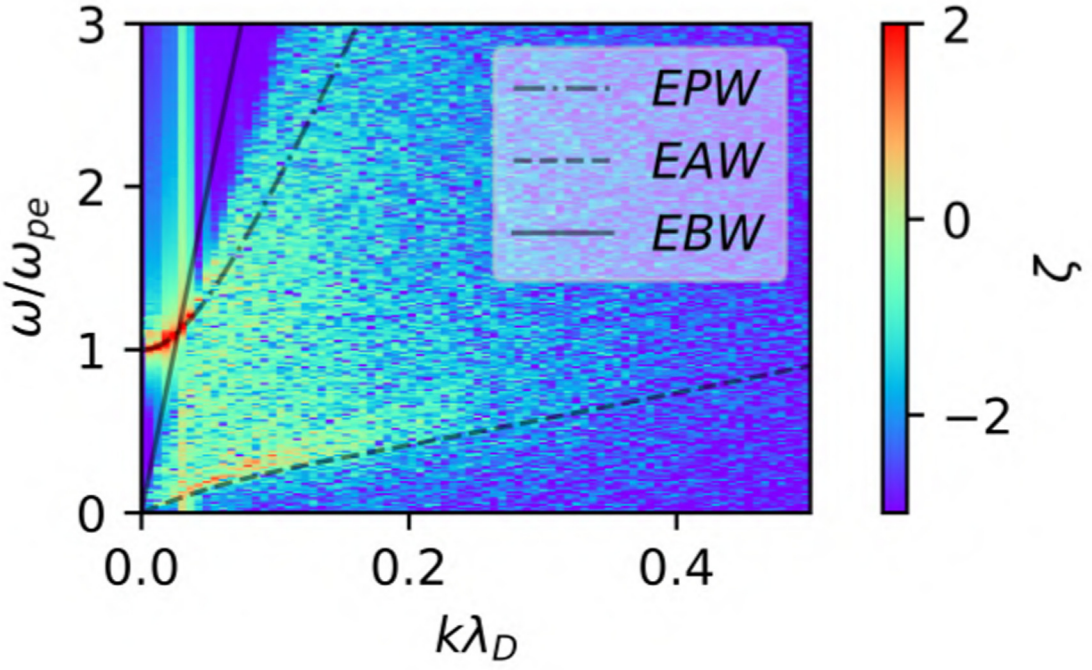

Fig. 7. Dispersion relation corresponding to Run-8 ($\alpha = 10, v_d = 40$). ζ represents the FFT amplitude of the normalized electric field.

hot (KE_H) and the cold electrons (KE_C) increase, a steadiness is set approximately beyond $\omega_{pe}t = 250$. The decay of the beam kinetic energy is not linear, rather oscillatory. There happens to be an insignificant but finite rise in the beam kinetic energy at an instance $\omega_{pe}t = 110$ (approx.). This rise will be further amplified for higher values of v_d. Fig. 3 shows the corresponding dispersion graph of the system. There are three modes that are supposed to be excited in the presence of a beam namely the Langmuir mode, electron acoustic mode and the beam mode (Lu et al. 2005; Koen et al. 2012). Out of these, the Langmuir mode or the electron plasma wave (EPW) is seen to be excited along

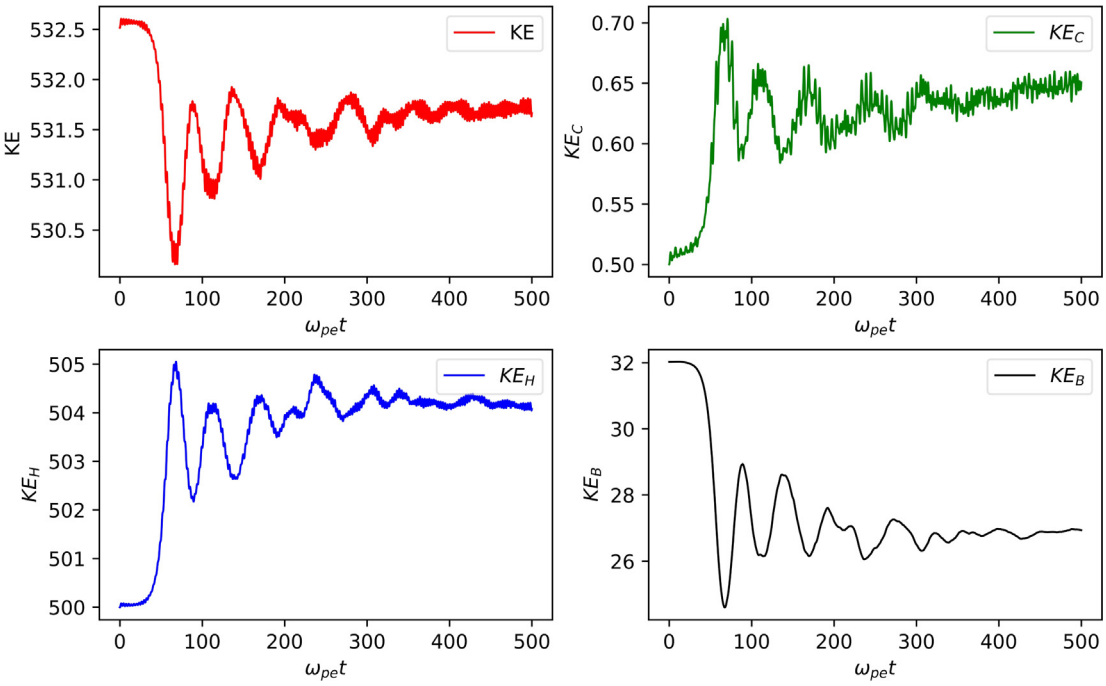

Fig. 8. Plot of the Kinetic Energy (in normalized unit) for Run-8. Here, KE denotes the total kinetic energy of the system, KE_C, KE_H and KE_B denote the kinetic energies of the cold, hot and beam electrons respectively.

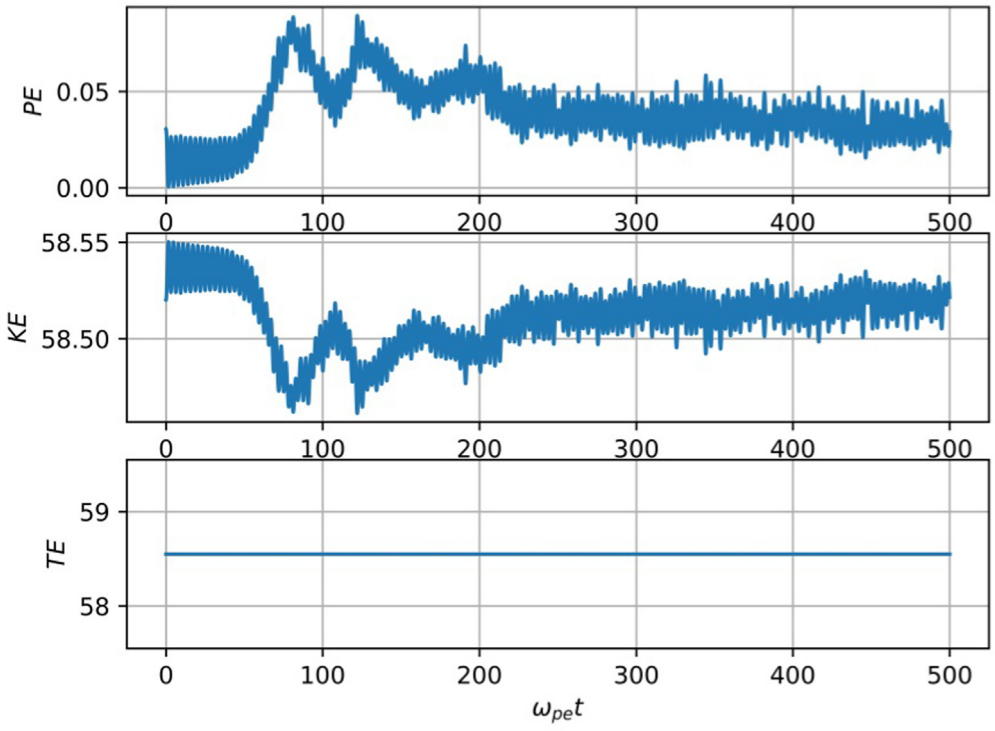

Fig. 9. Plot of the total Energy (in normalized unit) for $v_d = 20$. Here, *PE* stands for the potential energy, *KE* for kinetic energy and *TE* implies the total energy of the system.

with the electron acoustic wave (EAW). The electron beam wave (EBW), though not as prominent as the other two, is apparently present along the solid line. The beam mode may be captured well by increasing the spatial resolution of the system. In this and following dispersion plots, the negative values of the FFT amplitude is because of the log-

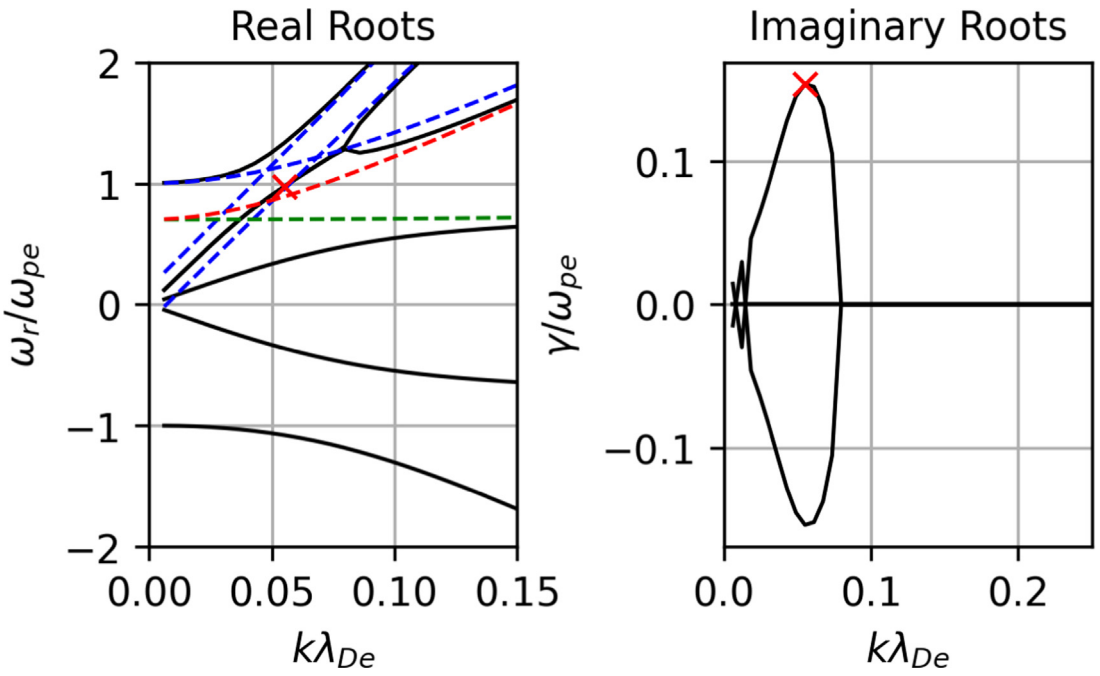

Fig. 10. Fluid dispersion plot for $v_d = 20$ corresponding to Run-2. The red and green lines represent the evolution of ω_{ph} and ω_{pc} respectively. The upper blue line represent ω_p(total electron plasma mode), while the blue dashed straight lines represent the two beam modes corresponding to two roots, in case only the third term of Eq. (11) prevails. These lines show the modal interactions and resulting instabilities. The cross symbol shows the fastest growing mode.

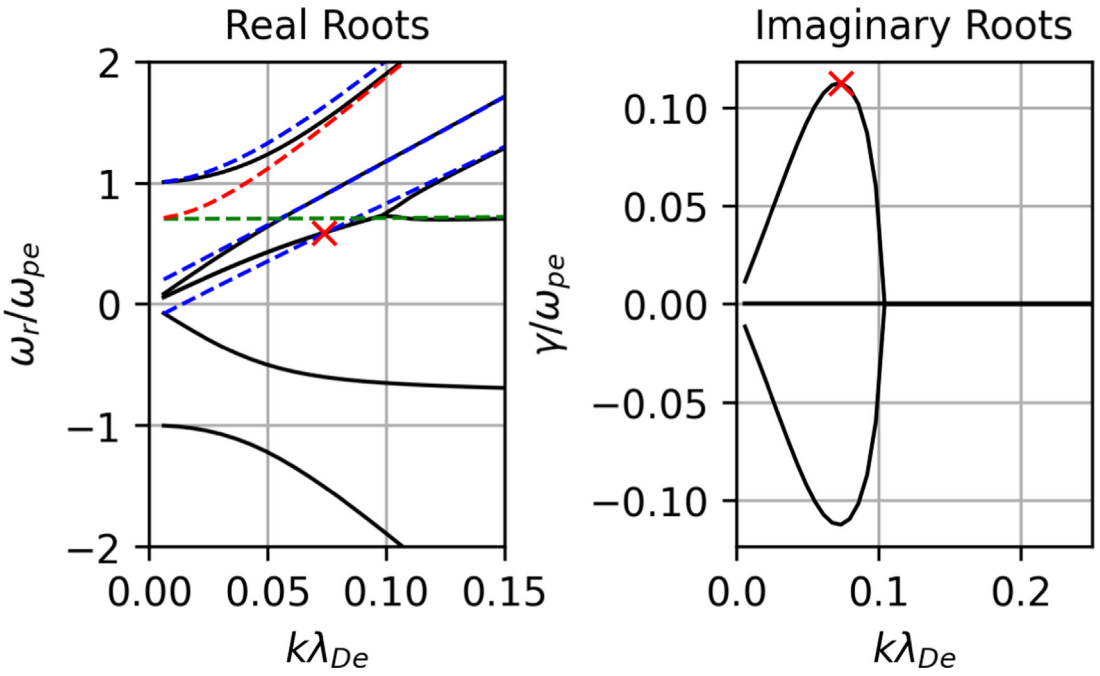

Fig. 11. Fluid dispersion plot for $v_d = 10$ and $\theta = T_h/T_c = 300$. Here, the lower beam mode interacts with the electron acoustic mode leading to the electron acoustic instability. The cross symbol shows the fastest growing mode.

arithmic scale of the absolute values of the electric field. Fig. 4 shows the kinetic energy plot for the whole system (KE) and three populations of electrons at a relatively high beam speed ($v_d = 80$). It is interesting to observe that, although there is a dissipation of the beam energy to the background electrons, the beam again receives back a portion of the energy from the hot and the cold species. Thus, in two consecutive instances, there is a bi-directional exchange of energy occurring between the beam and the other two species. This eventually gives rise to an oscilla-

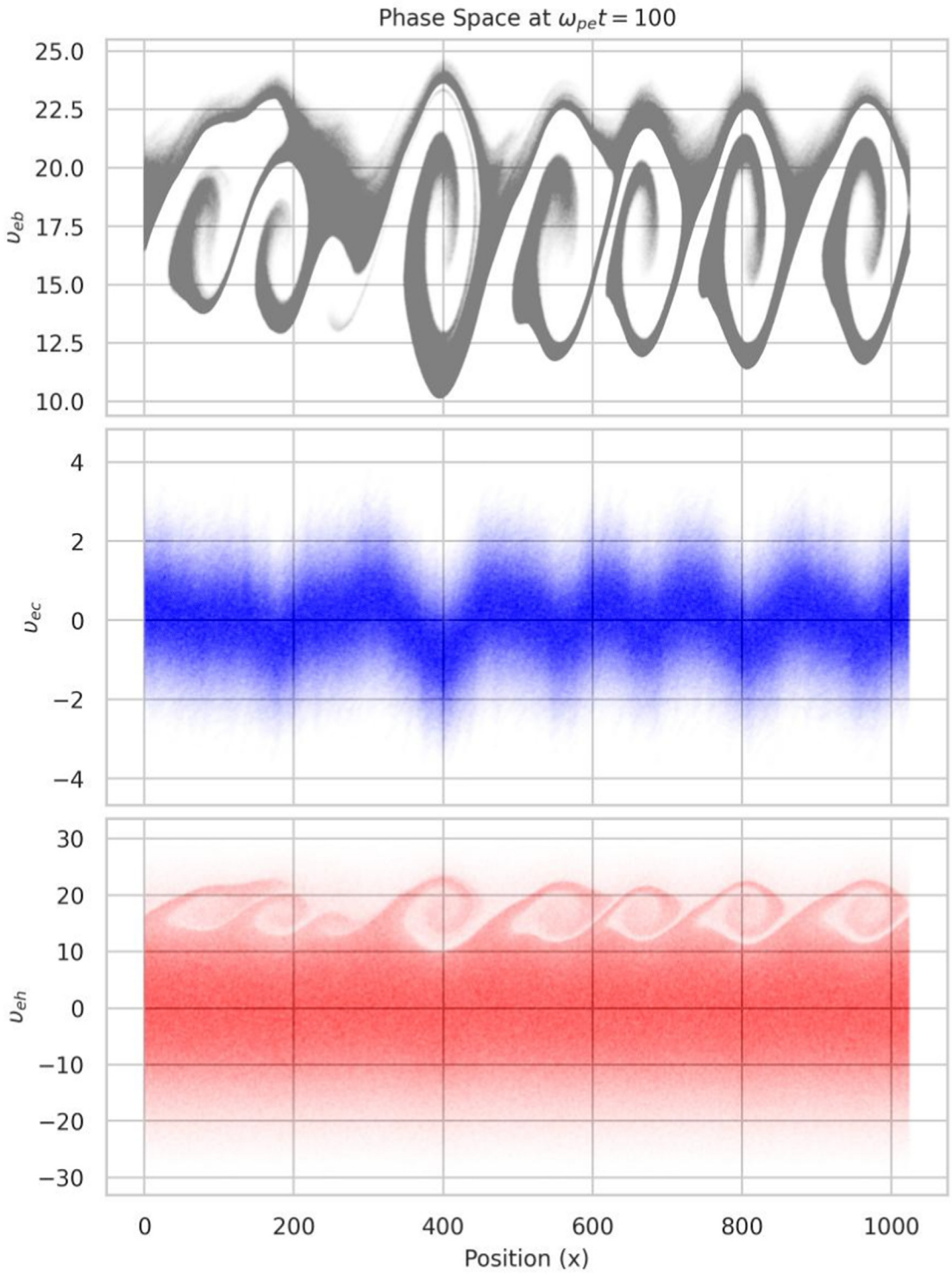

Fig. 12. Phase space plot at $v_d = 20$ for $\omega_{pe}t = 100$.

tory nature of the decay. Thus, there may be several instances where the beam regains a portion of the energy, but, the instance where the gain is maximum is interesting to observe. The dispersion plot of the resulting system is shown in Fig. 5. An important point here is that the electron acoustic mode is more damped as compared to the previous case (Fig. 3). In general, if the beam streaming speed is below the thermal speed of the hot electrons, the beam mode vanishes. However, above this limiting speed, the electron acoustic mode is amplified with a reduction in the beam energy (Gary and Tokar 1985; Lu et al. 2005). In Fig. 5, the beam energy is higher, and hence,

the electron acoustic mode is damped. The dispersion plot also captures the higher harmonics of the electron plasma wave and the electron acoustic wave.

At this point, it is important that we investigate the percentage retrieval of the beam kinetic energy and show the variation with v_d. By percentage retrieval we mean, the amount of energy retrieved by the beam from the background electrons at the instant of highest recovery (e.g. for $v_d = 80, \omega_{pe}t = 50$ approximately). Of course, the energy plots depict a gradual fall in the beam kinetic energy over time, but the instantaneous retrieval is of interest to us. Fig. 6 shows the overall percentage of the beam kinetic energy retrieval ($\Delta KE_B(\%)$) at different values of beam velocity (v_d). We observe an interesting trend with a sharp

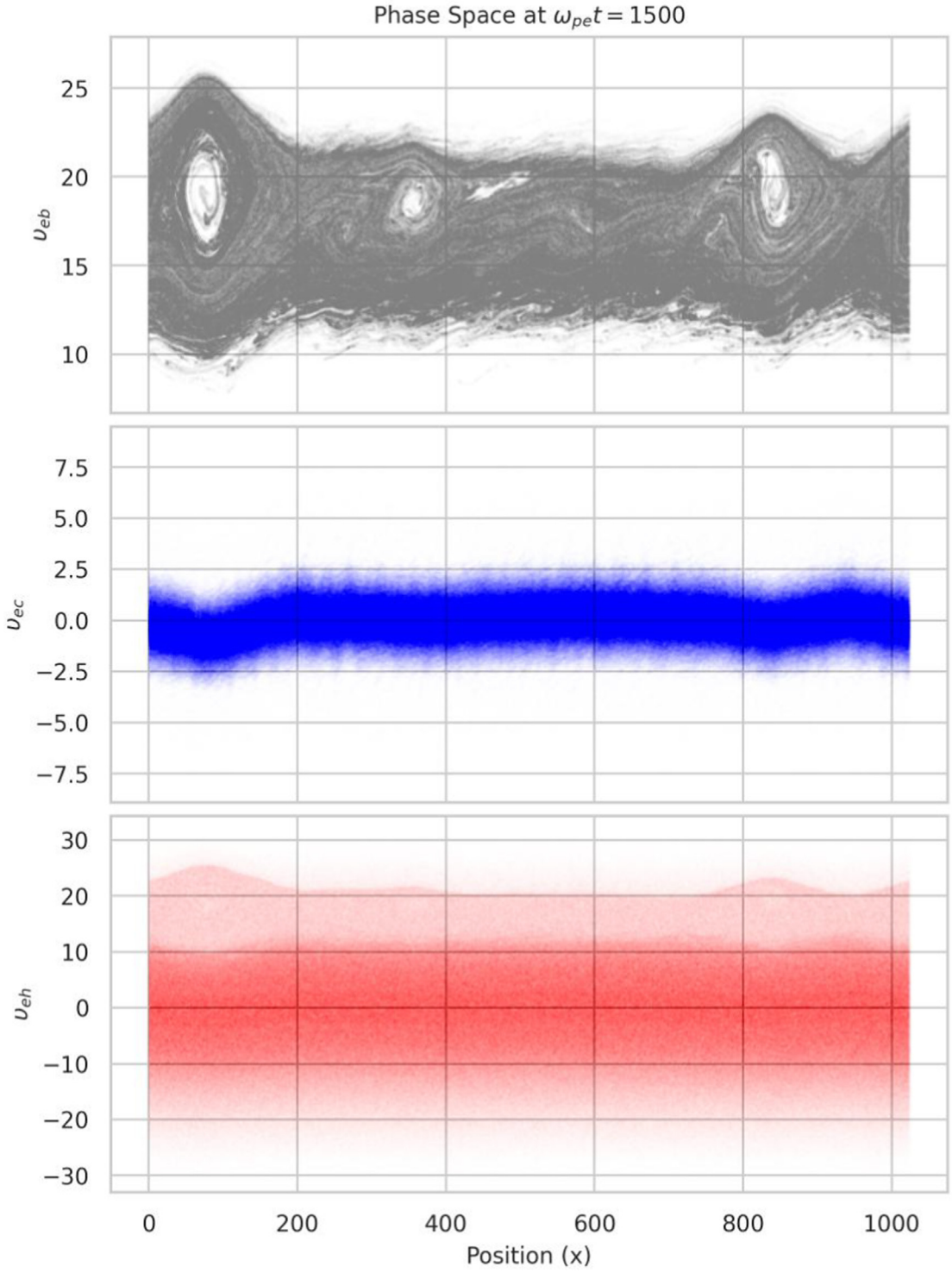

Fig. 13. Phase space plot at $v_d = 20$ for $\omega_{pe}t = 1500$.

rise in the energy retrieval from $v_d = 35$ to $v_d = 60$. Overall, the energy retrieval process seems to be non-linear with respect to the initial beam speed.

Fig. 7 and Fig. 8 show the dispersion graph and the kinetic energy profiles for $\alpha = 10$ (Run-8) respectively. In this case, the hot electron population is 10 times greater than the cold electron population. We observe a good agreement between the numerical and analytical expressions in the dispersion relation. The beam mode is not very prominent in this case. Furthermore, the electron acoustic waves appear only at lower values of k. It is worth noting that the Langmuir mode is independent of the parameter α

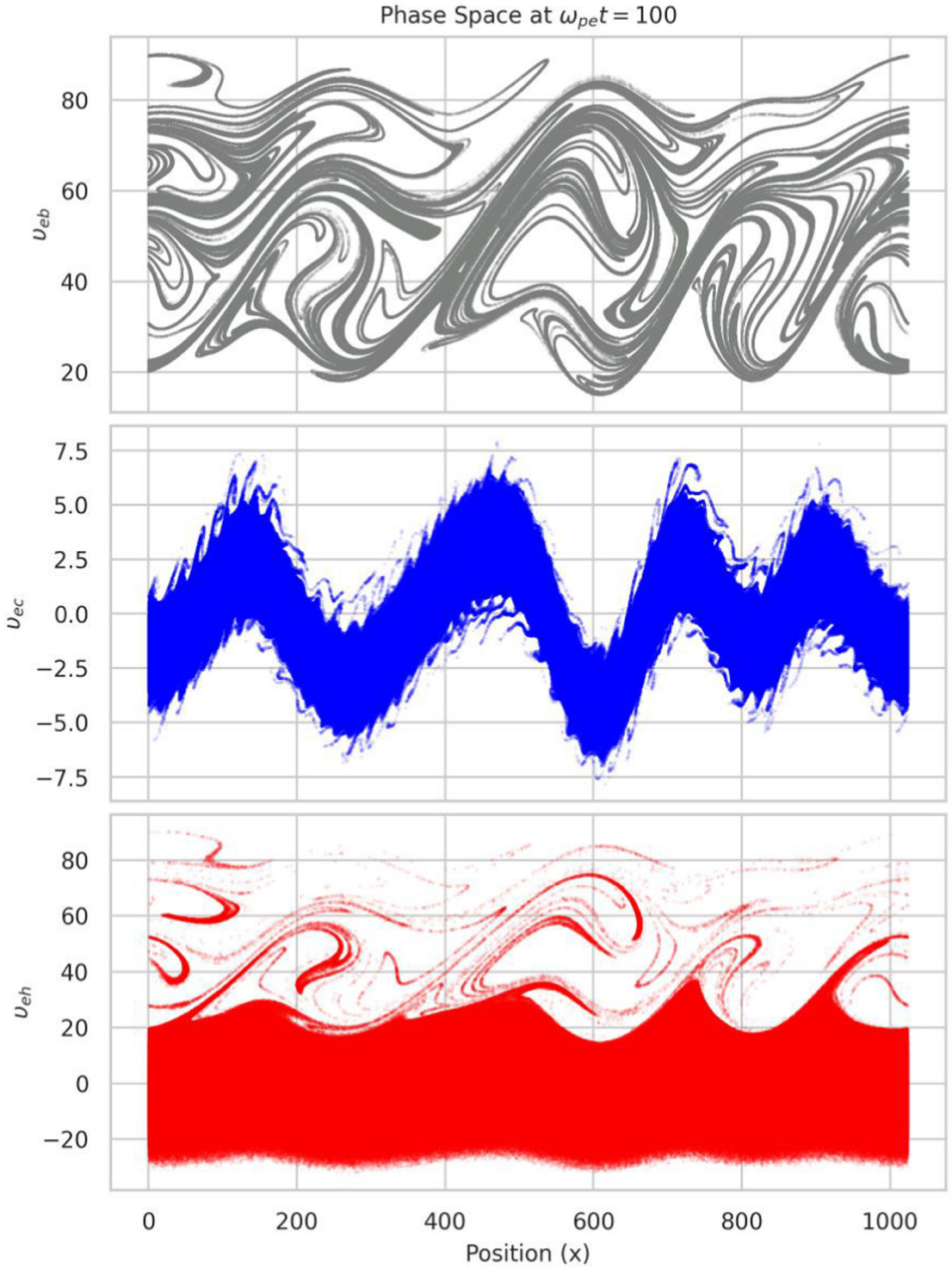

Fig. 14. Phase space plot at $v_d = 60$ for $\omega_{pe}t = 100$.

($\omega^2 = \omega_{pe}^2 + 3k^2[v_{Tc}^2 + v_{Th}^2]$). Thus, its shape and value shall not change with the increment of the hot electron density. On the other hand, the oscillatory nature of the beam energy decay becomes more prominent in this case. It is inferred that the hot electrons, being more responsive to the incoming beam, govern the beam energy decay. Thus, the hot electrons outperform the cold electrons in terms of the kinetic energy distribution. We further investigate the sum total of potential and kinetic energy of the system. Fig. 9 shows the total energy evolution of the system at $v_d = 20$. We observe that the potential and kinetic energy evolve opposite of each other, thereby keeping a constant

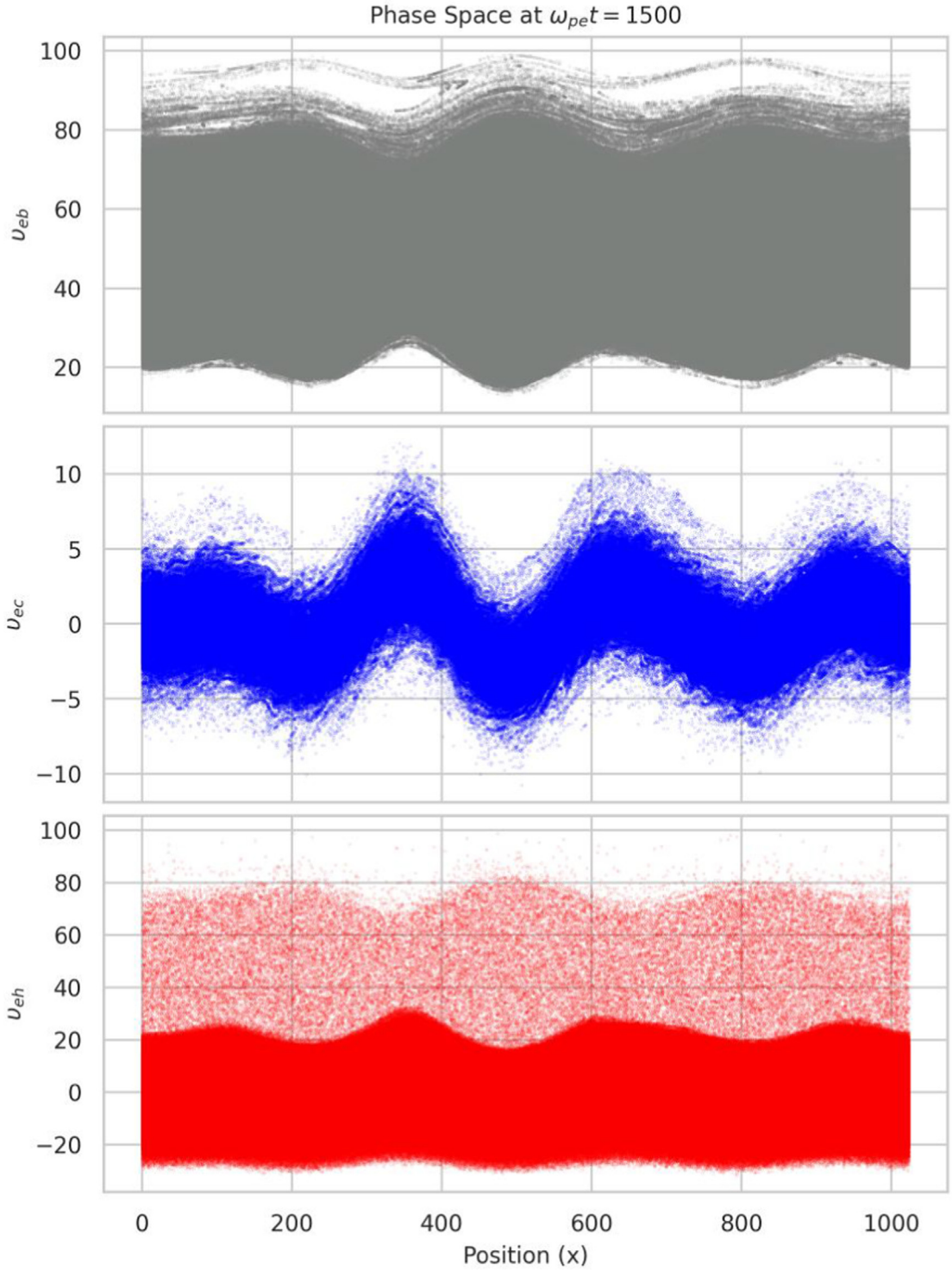

Fig. 15. Phase space plot at $v_d = 60$ for $\omega_{pe}t = 1500$.

total energy. This shows the conservation of energy in the system. For all other higher values of the parameter v_d, we observe a constant total energy. The electrostatic potential energy has been calculated using $U = \frac{\epsilon_0}{2}\int_v E^2 dv$, where, dv is a small element of volume and E is the electric field. It is important to note that generally the electrostatic PIC codes are either energy conserving or momentum conserving, but not both (Brackbill 2016; Pukhov 2015). In our case, the code is energy conserving. Though not conserved, total electron momentum varies around an average value with a low variation.

At this point it is important to highlight the interaction of the electron beam and the electron acoustic mode. Actually, the electron acoustic mode will be generated even without the presence of a beam (Gary and Tokar 1985). The presence of a beam is responsible for making the electron acoustic mode unstable. For the parameter regime of our simulation however, the electron beam mode is unstable due to its interaction with the electron plasma wave or Langmuir mode. The electron acoustic mode remains stable under these conditions since, the beam mode and the acoustic mode do not interact. However, with a rise in the hot electron temperature, the electron acoustic mode may become unstable due to its interaction with the beam. This fact can be established via the fluid dispersion relation given as follows:

$$\frac{\omega_{pc}^2}{\omega^2 - k^2 v_{Tec}^2} + \frac{\omega_{ph}^2}{\omega^2 - k^2 v_{Teh}^2} + \frac{\omega_{pb}^2}{(\omega - k v_0)^2 - k^2 v_{Teb}^2} = 1 \qquad (11)$$

A plot of this dispersion relation corresponding to the simulation Run-2 is given by the Fig. 10. A second plot for the same simulation parameters except for $v_d = 10$ and $\theta = T_h/T_c = 300$ is shown in Fig. 11. It is clear from both of these figures that the beam mode interacts with the Langmuir mode in the first case, while upon increasing the hot electron temperature and decreasing the beam velocity the beam mode interacts with the acoustic mode, eventually making it unstable.

Fig. 12 and Fig. 13 show the phase space plots of the beam, cold and hot electrons at two different instances ($\omega_{pe}t = 100$ and $\omega_{pe}t = 1500$) respectively for $v_d = 20$. While the first one shows the onset of instability, the second one is saturated. It can be easily observed (Fig. 12) that the hot electron vortices have smaller spread in velocity, however, approximately the same spatial size as the beam electrons. The beam has an overall positive velocity distribution. We consider the positive x-direction to be the motion of the beam. As the beam progresses, the hot electrons traveling in the same direction are significantly disturbed. The magnitude of the disturbance on the cold electrons is relatively weak. Once the instability is saturated, vortices merge together to form two major holes in the phase space (Fig. 13). These are often known as the Bernstein-Green-Kruskal (BGK) electron holes. Experimentally, these correspond to the solitary potential structures, which move at a speed much greater than the ion acoustic speed. Detailed analysis of BGK holes and electrostatic solitary structures may be found in Muschietti et al.

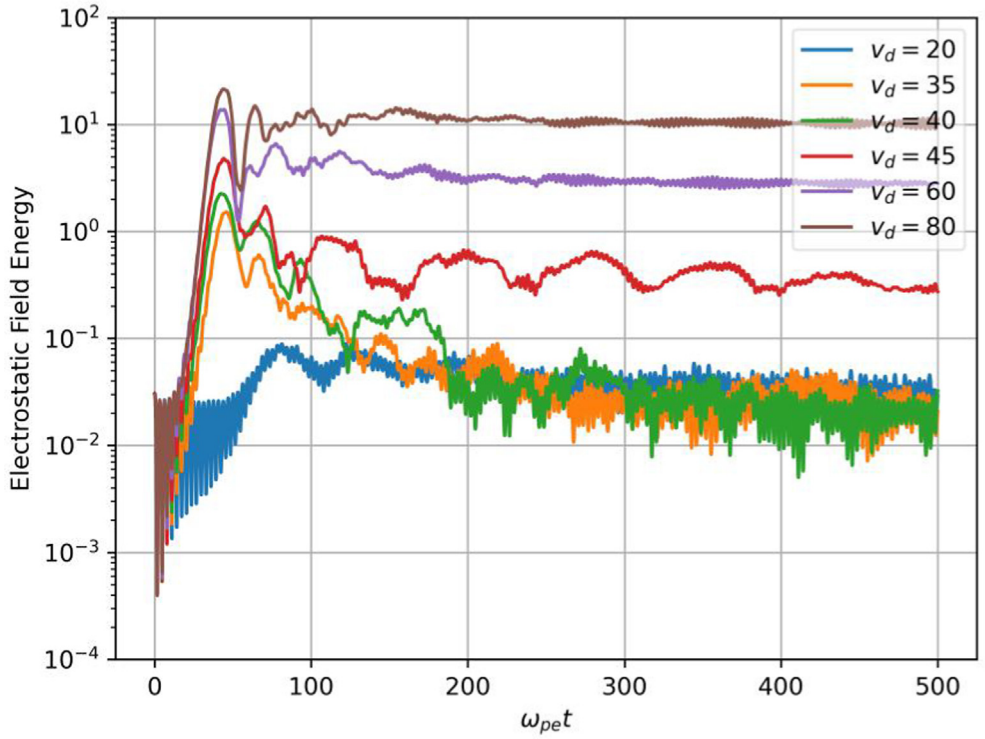

Fig. 16. Semi logarithm time history of the electrostatic field energy at different drift velocities.

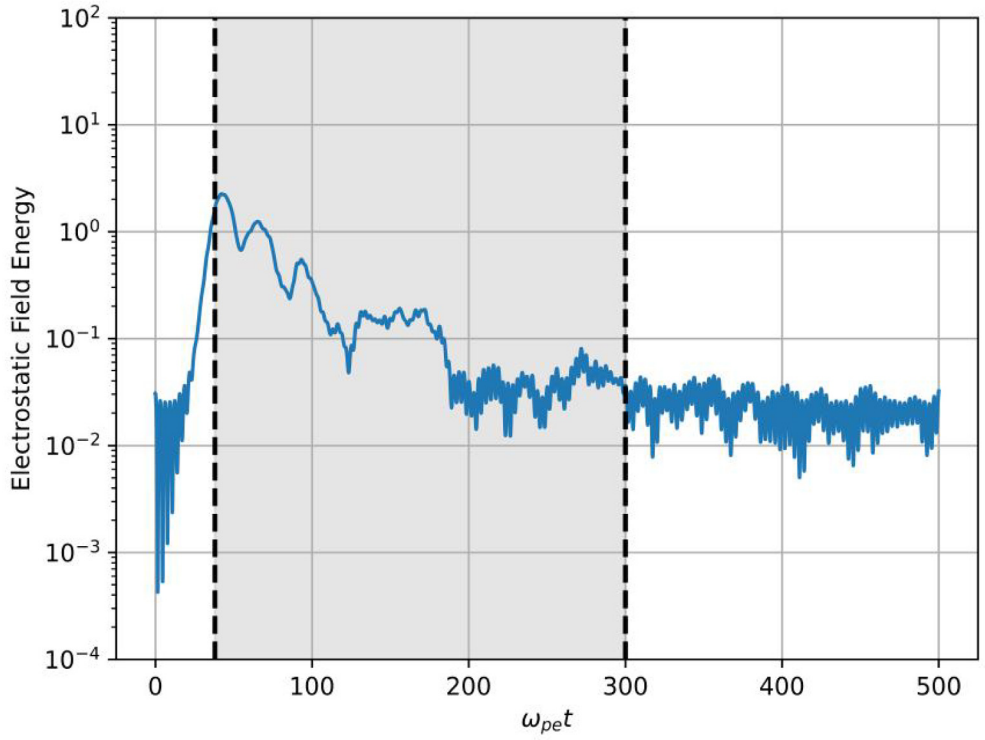

(a) Time history of electrostatic field energy (U) at v_d = 40

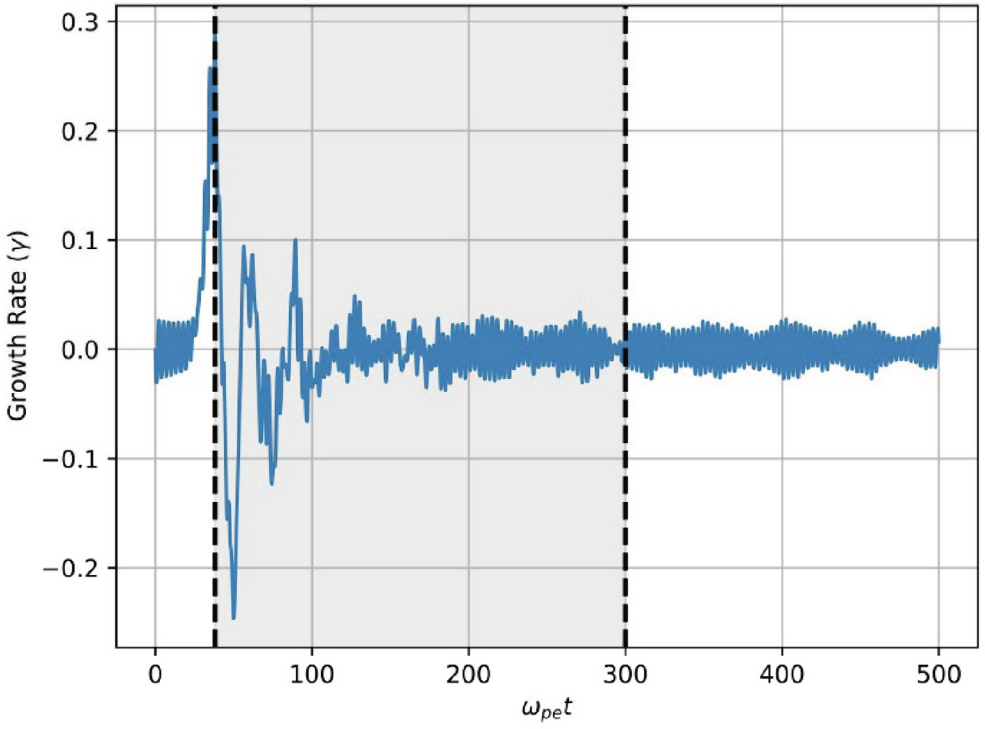

(b) Time history of the growth rate at v_d = 40

Fig. 17. Time history of the (a) electrostatic field energy (U) and (b) growth rate of streaming instability at $v_d = 40$.

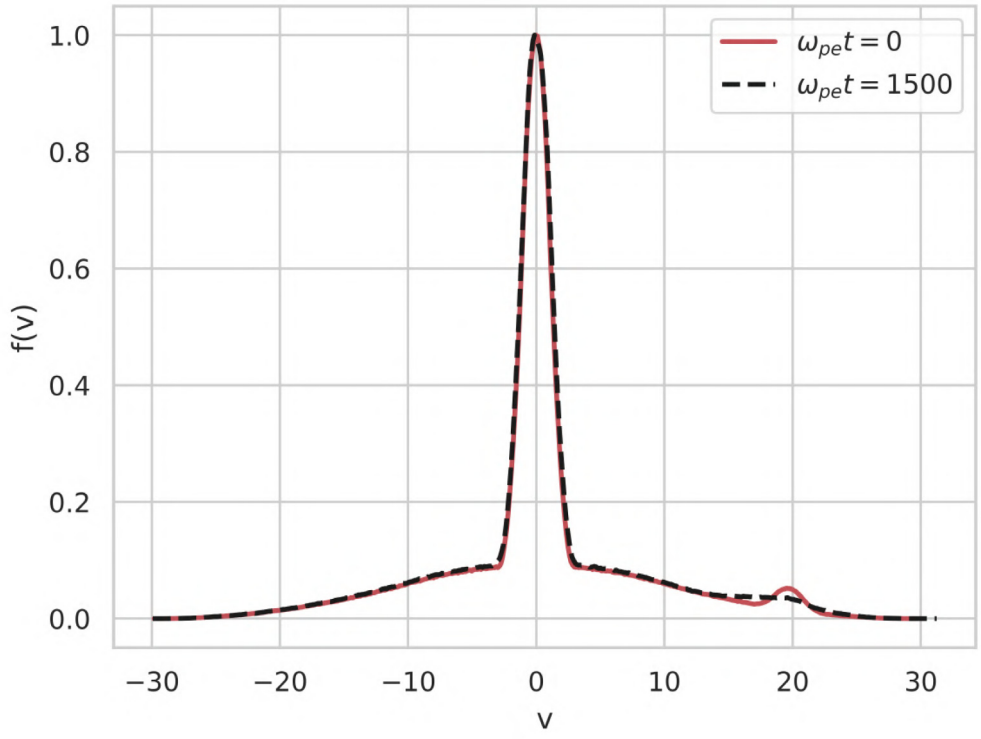

(a) v_d = 20

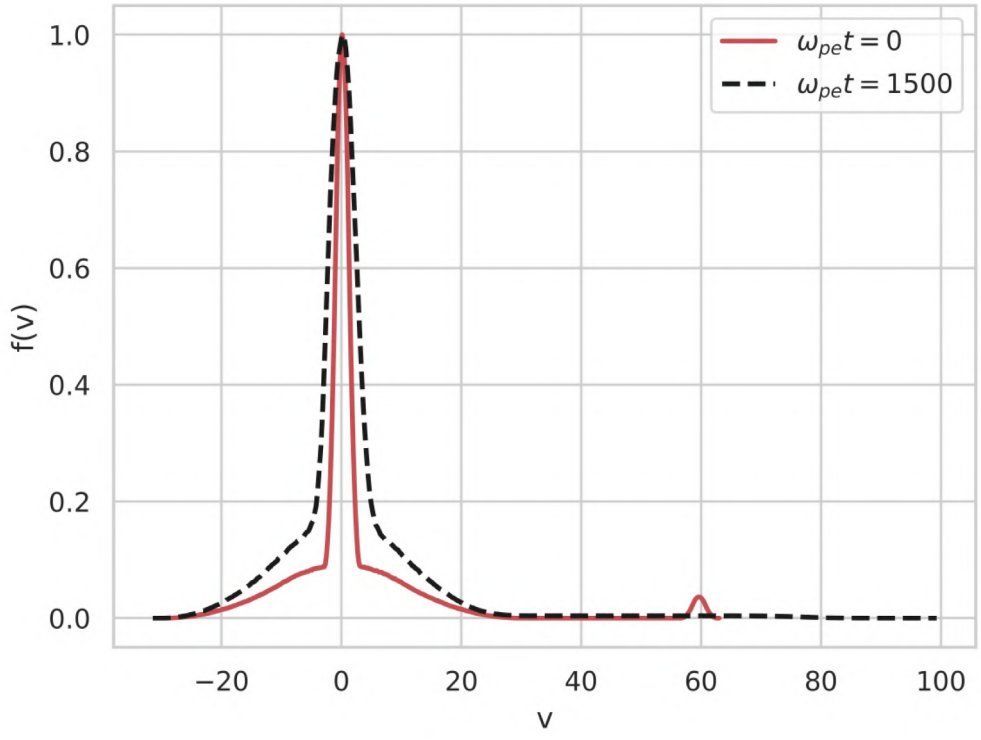

(b) v_d = 60

Fig. 18. Velocity distribution of the electrons for (a) $v_d = 20$ and (b) $v_d = 60$. The graph has been obtained from the particle data. The $f(v)$ has been re-normalized in the plot with its maximum value to find a scale between 0 and 1. The graphs show the initial and final distributions.

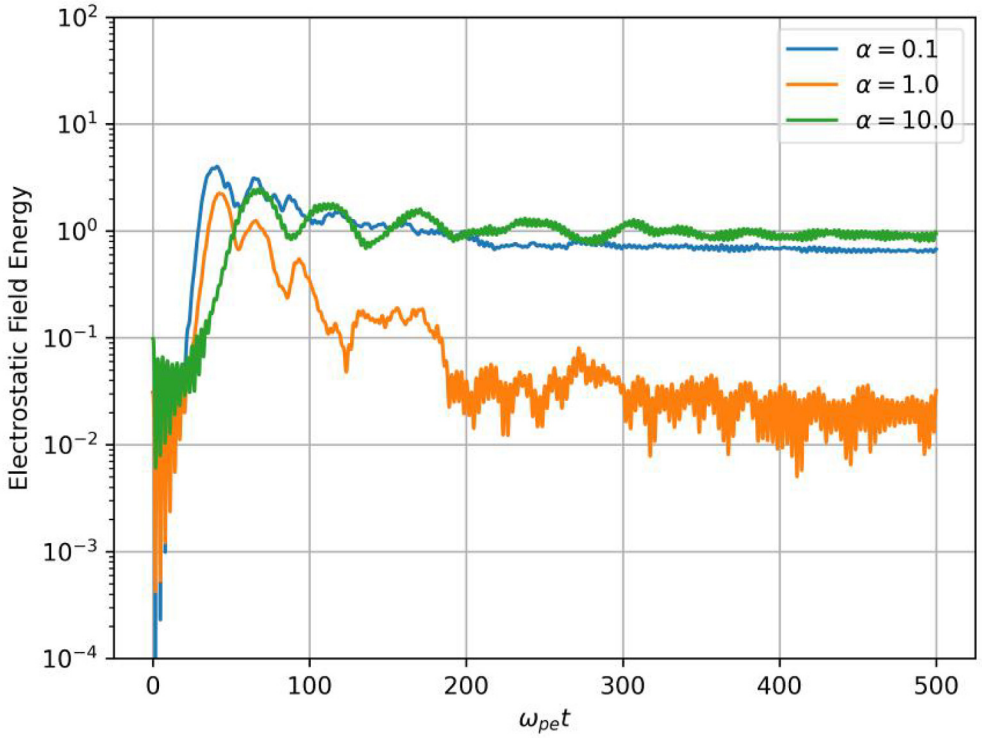

(a) Electrostatic field energy at different values of α, corresponding to Run-5, Run-8 and Run-9

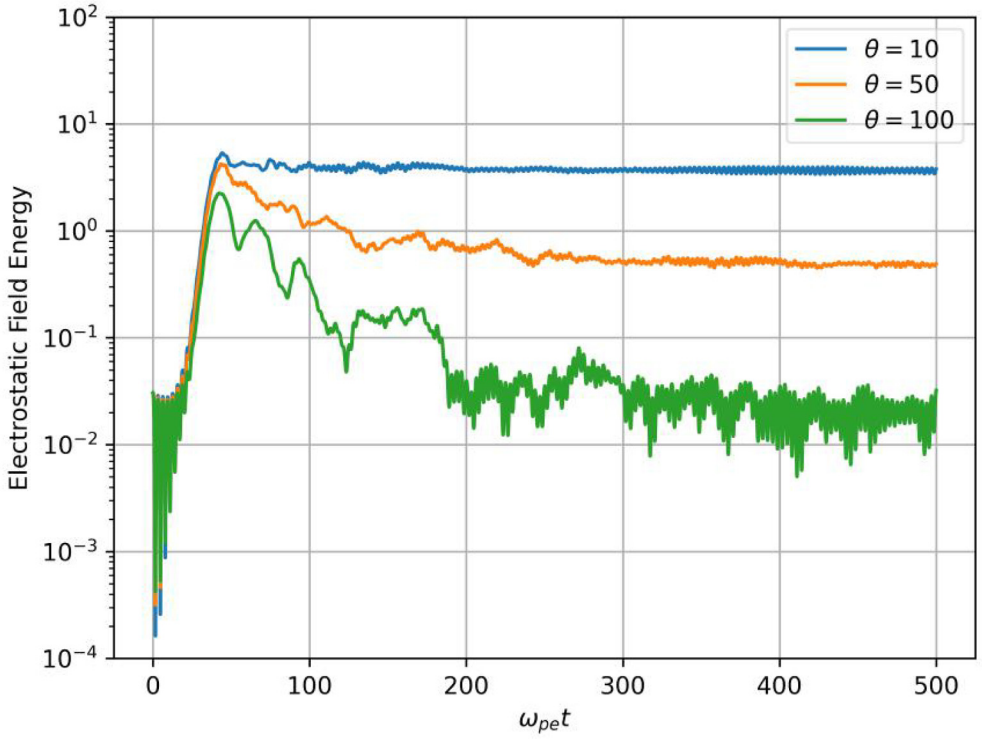

(b) Electrostatic field energy at different values of θ, corresponding to Run-5, Run-10 and Run-11

Fig. 19. Semi logarithm time history of the electrostatic field energy (a) at different values of α and (b) at different values of θ.

(1999); Hutchinson (2017); Omura et al. (1994). The fact that electron beams are responsible for the generation of electrostatic solitary waves has been reported in some previous works (Omura et al. 1996; Jao and Hau 2016; Jao and Hau 2014; Miyake et al. 1998; Miyake et al. 2000; Singh et al. 2000). Fig. 14 and Fig. 15 on the other hand show the phase space at those two instances for higher beam velocity ($v_d = 60$). With higher beam velocity, hot electrons are seen to form stronger vortices. In addition, the vortex size of the beam is also enhanced. There seems to be a good correlation between the spatial sizes of the hot and beam electron vortices.

In order to analyze the instability, Fig. 16 shows the time history plot of the electrostatic field energy for different beam speed. From the figure we find an estimate of the linear growth, non-linear evolution and saturation stage of the streaming instability. On a gross scale, the time history evolution may be classified into three different stages, the linear instability phase, oscillatory decay phase, and the saturation phase (Miyake et al. 2000). The oscillatory decay phase is the non-linear phase of evolution of the instability. Occurrence of these phases varies with the beam speed. The corresponding growth rate of the instability may be written as (Lotov et al. 2009):

$$\gamma = \partial ln(U)/\partial t$$

Fig. 17 shows a plot of the electrostatic field energy and growth rate for $v_d = 40$. As the instability develops, we observe the linear growth phase till $\omega_{pe}t = 38$ (approx.), beyond which the instability goes through a non-linear phase of decay and oscillation (or striations) till $\omega_{pe}t = 300$, eventually leading to saturation. For higher beam speed, the saturation phase seems to appear early, reducing the oscillatory phase. In general, the formation of phase space holes and the growth of the associated electric potentials trap the electrons during the linear phase of the instability. For a low beam speed, such potentials merge over time forming the electrostatic solitary wave (ESW), which is a type of Bernstein, Greene, and Kruskal (BGK) mode (Hutchinson 2017). In the case of three electron populations (refer Fig. 12), the phase space holes are mostly observed to be formed by the beam electrons. The BGK modes represent the non-linear electrostatic waves, and trapped particles are crucial for sustaining these modes. Non-linear saturation of two-stream instability is responsible for the generation of such modes (Lakhina et al. 2021). Since the beams carry the initial kinetic energy of the system, as soon as they are trapped, this energy is converted into the field energy, giving rise to the linear growth. Since the hot electrons receive the major part of the beam kinetic energy, they are also trapped in the same fashion by the emerging potentials. The cold electrons on the other hand respond to the potentials due to the holes, but they do not form the holes unlike the beam and hot species.

Fig. 18 shows the velocity distribution of the overall electron population at two time instances for $v_d = 20$ and $v_d = 60$ respectively. While $\omega_{pe}t = 0$ implies the initial velocity distribution, $\omega_{pe}t = 1500$ represents the much later stage of saturation of the instability. For the low beam speed ($v_d = 20$), there is no gap in the distribution of the background electrons (hot & cold) and the beam. The situation is much alike the bump-on-tail instability as described in Omura et al. (1996). For higher beam speeds (such as $v_d = 60$), there is a gap in the distribution function of the beam and the background electrons, which is alike the weak beam instability. In both of these cases, the background electrons are the major group while the beam constitutes the minority group. Thus, there is non-linear trapping of the minor electrons (i.e. the beam electrons) for both of these cases. However, in order to generate and sustain the electrostatic solitary waves (ESW), the following inequality has to be satisfied (Omura et al. 1996).

$$f_1(v_x) > f_d(v_x) \; where, \; v_x = \frac{\omega}{k} - V_T \tag{12}$$

Here, f_1 represents the initial distribution of the hot electrons, f_d is the diffused beam distribution, V_T represents the trapping velocity range and ω/k is the phase velocity of the wave corresponding to the maximum growth. To evaluate the inequality we shall need further expressions which are to be found in Omura et al. (1996). In Fig. 18, the sharp peaked region of the distribution is due to the cold electrons, while the flattened region is due to the hot electrons. Thus, the bump of beam occurs at the high energy tail of the hot electrons. Therefore, we consider only the hot electrons and the beam for the evaluation of the inequality. Upon evaluation, we find the inequality to hold good for $v_d = 20$. In fact the inequality holds up to $v_d = 38$. Beyond this, the inequality does not hold well. Hence, it may be concluded that for $v_d <= 38$, the instability being alike bump on tail, ESW is supported, while for $v_d > 38$, the instability is alike weak beam, and due to the invalidation of the inequality, ESW is not supported. Thus, $v_d = 38$ acts as the threshold value for sustaining the ESW. Physically, for the bump-on-tail instability, the most unstable Langmuir mode destroys the positive gradient of the distribution function completely and there occurs no further trapping of the electrons by other modes having a different phase velocity. The non-linear trapping is limited to a single phase velocity corresponding to a monochromatic wave. Thereby, the trapping potentials coalesce to form the ESW (Omura et al. 1996). Quite contrary to this, for the weak beam instability, since the beam electrons diffuse to meet the velocity gap in the distribution function, the positive gradient cannot be destroyed by a monochromatic wave. There are subsequent excitations of Langmuir waves of different phase velocities and each of them is responsible for trapping a certain portion of the beam electrons. Therefore, there is no coalescence of the potential structures and consequently no ESW is excited. For the weak beam instability, both beam and hot electrons are trapped. We also observe small vortex formation in the velocity edges of the cold electrons for higher beam speed. In both these type

of instabilities we have not observed any role of the cold ion motion, as has been mentioned in Omura et al. (1996). As a distinct difference with Omura et al. (1996), we have observed the background hot electrons to be trapped along with the beam electrons for a weak beam instability.

It is interesting to note that the non-linear decay process of the instability often has an associated oscillating or striation phase just before saturation. This can be explained following Miyake et al. (2000); Hou et al. (2015), which say, the electrons remain in BGK equilibrium with one of the potentials. As they move into the adjacent potential, they disturb the balance between the electrons and potentials. The newly trapped electrons in the potential oscillate back and forth, to mix with the original electrons of that potential, eventually forming a new BGK equilibrium. This process raises and decays the overall field energy giving rise to the striations.

Fig. 19 shows the time evolution of the electrostatic field energy at different values of α and θ respectively. We observe a quasi-step before reaching the saturation, when $\alpha = 1.0$. For the cases, where, the concentrations of hot and cold electrons vary (i.e. $\alpha = 0.1\&10$), the instability passes through a quick non-linear phase to saturation. In addition, the linear growth times also increase, as the order of α increases. On the other hand, at relatively low hot to cold electron temperature ratio ($\theta = 10$), there seems to be only two stages of the instability - the linear instability stage followed by saturation. As the hot electron temperature is raised, the instability passes through the quasi step non-linear phase until saturation.

4. Conclusions

The paper aims at understanding the electron dynamics and its effects on the Earth's ionosphere. The region is rich in non-linear dynamical phenomena. Mutual interactions of the hot and cold electrons in the presence of a beam have portrayed several interesting facts. The following are some of the critical observations:

1. It has been observed that the kinetic energy plays an important role. Usually, there is a dominant energy transfer from the beam to the other species of electrons, however, at high beam energies, a portion of the energy is instantaneously regained by the beam from the other electron species. This is essentially a part of the non-linear decay process of the instability. This retrieval is non-linearly related to the initial beam energy, although, we see a sharp and almost linear transition from $v_d = 35$ to $v_d = 60$.
2. The hot electrons are more responsive to the incoming beam and are trapped along with them in almost every situation. The spatial vortex sizes of the beam and hot electrons are highly correlated.
3. The time history of the electrostatic field energy has been analyzed for a wide variety of parameters. For most of the cases it has been found that the instability passes through three distinct phases, namely the linear growth, oscillatory decay and saturation. However, for a comparatively low hot electron temperature, there are apparently two phases- linear growth and saturation. Moreover, the passage through different phases is also affected by the relative concentrations of the hot and cold electrons.
4. Evaluation of the condition for the supported ESW has revealed a threshold value of $v_d = 38$, beyond which the BGK modes or ESWs are not supported by the non-linear saturation phase of the instability.

Thus, the paper has conclusively described the profile of kinetic energy and its initial retrieval by the beam, depending on the beam velocity; commented on the critical velocity of the beam for sustained electrostatic solitary waves along with an analysis of the instability. Effect of increasing density and temperature ratio of hot to cold electrons on the saturation of the instability has also been addressed. We believe that such a systematic analysis of this system has not been done previously and the results would add new information to this field of study.

Acknowledgments

The simulations for the work described in this paper were performed on **ANTYA**, an HPC Linux Cluster, IPR, Gujarat, India. WJM acknowledges funding from the European Research Council (ERC) under the European Union's Horizon 2020 research and innovation programme (ERC Consolidator Grant agreement No. 866357, POLAR-4DSpace).

References

An, X., Bortnik, J., Van Compernolle, B., et al., 2017. Electrostatic and whistler instabilities excited by an electron beam. Physics of Plasmas 24 (7), 072116. https://doi.org/10.1063/1.4986511.

Birdsall, C.K., Langdon, A.B., 2004. Plasma physics via computer simulation. CRC Press. https://doi.org/10.1201/9781315275048.

Bohm, D., Gross, E.P., 1949. Theory of plasma oscillations. B. excitation and damping of oscillations. Physical Review 75 (12), 1864. https://doi.org/10.1103/PhysRev.75.1864.

Brackbill, J.U., 2016. On energy and momentum conservation in particle-in-cell plasma simulation. Journal of Computational Physics 317, 405–427. https://doi.org/10.1016/j.jcp.2016.04.050.

Brask, S.M., Marholm, S., Di Mare, F., et al., 2022. Electron–neutral collisions effects on langmuir probe in the lower e-region ionosphere. Physics of Plasmas 29 (3), 033511. https://doi.org/10.1063/5.0079761.

Brieda, L., 2019. Plasma Simulations by Example. CRC Press, URL: https://www.routledge.com/Plasma-Simulations-by-Example/Brieda/p/book/9780429439780.

Chakrabarti, N., Sengupta, S., 2009. Nonlinear interaction of electron plasma waves with electron acoustic waves in plasmas. Physics of Plasmas 16 (7), 072311. https://doi.org/10.1063/1.3191722.

Changmai, S., Bora, M.P., 2019. Photoemission driven electron two-stream instability (ETSI) and evolution of plasma sheath. Physics of Plasmas 26 (4), 042113. https://doi.org/10.1063/1.5081928.
Cowley, S.W.H. 2007. Magnetosphere of the Earth. In D. Gubbins, & E. Herrero-Bervera (Eds.), Encyclopedia of Geomagnetism and Paleomagnetism (pp. 656–664). Dordrecht: Springer, Netherlands. https://doi.org/10.1007/978-1-4020-4423-6_205.
Crary, F., Goldman, M., Ergun, R., et al., 2001. Explanation for the simultaneous occurrence of bipolar structures and waves near ion-cyclotron harmonics in the auroral ionosphere. Geophysical Research Letters 28 (15), 3059–3062. https://doi.org/10.1029/2001GL013050.
Dalgarno, A., McElroy, M.B., Moffett, R., 1963. Electron temperatures in the ionosphere. Planetary and Space Science 11 (5), 463–484. https://doi.org/10.1016/0032-0633(63)90071-0.
DuBois, A.M., Thomas Jr, E., Amatucci, W.E., et al., 2014. Experimental characterization of broadband electrostatic noise due to plasma compression. Journal of Geophysical Research: Space Physics 119 (7), 5624–5637. https://doi.org/10.1002/2014JA020198.
Dum, C., 1990. Simulation studies of plasma waves in the electron foreshock: The transition from reactive to kinetic instability. Journal of Geophysical Research: Space Physics 95 (A6), 8111–8122. https://doi.org/10.1029/JA095iA06p08111.
Garrett, H.B., Kim, W., Evans, R.W., 2016. Updating the jovian plasma and radiation environments: The latest results for 2015. Journal of Spacecraft and Rockets 53 (4), 693–707. https://doi.org/10.2514/1.A33510.
Gary, S.P., Tokar, R.L., 1985. The electron-acoustic mode. The Physics of Fluids 28 (8), 2439–2441. https://doi.org/10.1063/1.865250.
Ginzburg, V., Zhelezniakov, V., 1958. On the possible mechanisms of sporadic solar radio emission (radiation in an isotropic plasma). Soviet Astronomy 2, 653, URL: https://ui.adsabs.harvard.edu/abs/1958SvA....2.653G.
Goldman, M.V., Crary, F., Newman, D.L., et al., 2000. Turbulence driven by two-stream instability in a magnetized plasma. Physics of Plasmas 7 (5), 1732–1739. https://doi.org/10.1063/1.873992.
Henri, P., Califano, F., Briand, C., et al., 2010. Vlasov-Poisson simulations of electrostatic parametric instability for localized Langmuir wave packets in the solar wind. Journal of Geophysical Research: Space. Physics 115 (A6), A06106, https://doi.org/10.1029/2009JA014969.
Holman, G., & Benedict, S. ( ). Solar flare theory. URL: https://hesperia.gsfc.nasa.gov/sftheory/toc.htm.
Hou, Y., Chen, M., Yu, M., et al., 2015. Linear and nonlinear behaviour of two-stream instabilities in collisionless plasmas. Journal of Plasma Physics 81 (6), 905810602. https://doi.org/10.1017/S0022377815001087.
Hutchinson, I.H., 2017. Electron holes in phase space: What they are and why they matter. Physics of Plasmas 24 (5), 055601. https://doi.org/10.1063/1.4976854.
Jao, C.-S., Hau, L.-N., 2014. Electrostatic solitary waves and hole structures generated by bump-on-tail instability in electron-positron plasmas. Physical Review E 89 (5), 053104. https://doi.org/10.1103/PhysRevE.89.053104.
Jao, C.-S., Hau, L.-N., 2016. Fluid theory and kinetic simulation of two-dimensional electrostatic streaming instabilities in electron-ion plasmas. Physics of Plasmas 23 (11), 112110. https://doi.org/10.1063/1.4967283.
Karak, B.B., Mandal, S., Banerjee, D., 2018. Double peaks of the solar cycle: an explanation from a dynamo model. The Astrophysical Journal 866 (1), 17. https://doi.org/10.3847/1538-4357/aada0d.
Kasaba, Y., Matsumoto, H., Omura, Y., 2001. One-and two-dimensional simulations of electron beam instability: Generation of electrostatic and electromagnetic 2fp waves. Journal of Geophysical Research: Space Physics 106 (A9), 18693–18711. https://doi.org/10.1029/2000JA000329.
Khazanov, G.V., Chen, M.W., Lemon, C.L., et al., 2019. The magnetosphere-ionosphere electron precipitation dynamics and their geospace consequences during the 17 March 2013 storm. Journal of Geophysical Research: Space Physics 124 (8), 6504–6523. https://doi.org/10.1029/2019JA026589.
Koen, E.J., Collier, A.B., Maharaj, S.K., 2012. Particle-in-Cell simulations of beam-driven electrostatic waves in a plasma. Physics of Plasmas 19 (4), 042101. https://doi.org/10.1063/1.3695402.
Lakhina, G.S., Singh, S., Rubia, R., et al., 2021. Electrostatic solitary structures in space plasmas: Soliton perspective. Plasma 4 (4), 681–731. https://doi.org/10.3390/plasma4040035.
Langley, R.B., 2000. GPS, the Ionosphere, and the Solar Maximum. GPS World 11 (7), 44–49, URL: https://chain-new.chain-project.net/images/docs/gpsworld-july2000.pdf.
Lin, C., Burch, J., Shawhan, S., et al., 1984. Correlation of auroral hiss and upward electron beams near the polar cusp. Journal of Geophysical Research: Space Physics 89 (A2), 925–935. https://doi.org/10.1029/JA089iA02p00925.
Lotov, K., Terekhov, A., Timofeev, I., 2009. Saturation of two-stream instability of an electron beam in plasma. Plasma Physics Reports 35, 518–525. https://doi.org/10.1134/S1063780X09060099.
Lu, Q., Wang, S., Dou, X., 2005. Electrostatic waves in an electron-beam plasma system. Physics of Plasmas 12 (7), 072903. https://doi.org/10.1063/1.1951367.
Marif, H., Lilensten, J., 2020. Suprathermal electron moments in the ionosphere. Journal of Space Weather and Space Climate 10, 22. https://doi.org/10.1051/swsc/2020021.
Mbuli, L., Bharuthram, R., Maharaj, S., 2018. The effect of a warm electron beam on slow electron-acoustic solitons. Physics of Plasmas 25 (1), 012318. https://doi.org/10.1063/1.5002095.
Miyake, T., Omura, Y., Matsumoto, H., 2000. Electrostatic particle simulations of solitary waves in the auroral region. Journal of Geophysical Research: Space Physics 105 (A10), 23239–23249. https://doi.org/10.1029/2000JA000001.
Miyake, T., Omura, Y., Matsumoto, H., et al., 1998. Two-dimensional computer simulations of electrostatic solitary waves observed by Geotail spacecraft. Journal of Geophysical Research: Space Physics 103 (A6), 11841–11850. https://doi.org/10.1029/98JA00760.
Muschietti, L., Roth, I., Ergun, R., et al., 1999. Analysis and simulation of BGK electron holes. Nonlinear Processes in Geophysics 6 (3/4), 211–219. https://doi.org/10.5194/npg-6-211-1999.
Newman, D., Goldman, M., Ergun, R., et al., 2001. Formation of double layers and electron holes in a current-driven space plasma. Physical Review Letters 87 (25), 255001. https://doi.org/10.1103/PhysRevLett.87.255001.
IRI, URSI/COSPAR W.G. (2023). International reference ionosphere. URL: https://ccmc.gsfc.nasa.gov/models/IRI~2016/
NOAA (2023). Space Weather Prediction Center solar cycle progression. URL: https://www.swpc.noaa.gov/products/solar-cycle-progression.
Norgren, C., Graham, D.B., Argall, M., et al., 2022. Millisecond observations of nonlinear wave–electron interaction in electron phase space holes. Physics of Plasmas 29 (1), 012309. https://doi.org/10.1063/5.0073097.
Omura, Y., Kojima, H., Matsumoto, H., 1994. Computer simulation of electrostatic solitary waves: A nonlinear model of broadband electrostatic noise. Geophysical Research Letters 21 (25), 2923–2926. https://doi.org/10.1029/94GL01605.
Omura, Y., Matsumoto, H., Miyake, T., et al., 1996. Electron beam instabilities as generation mechanism of electrostatic solitary waves in the magnetotail. Journal of Geophysical Research: Space Physics 101 (A2), 2685–2697. https://doi.org/10.1029/95JA03145.
Parks, G.K., 2019. Physics of space plasmas: An introduction. CRC Press.
Pottelette, R., Ergun, R., Treumann, R., et al., 1999. Modulated electron-acoustic waves in auroral density cavities: FAST observations. Geophysical Research Letters 26 (16), 2629–2632. https://doi.org/10.1029/1999GL900462.
Pukhov, A. 2015. Particle-in-Cell codes for plasma-based particle acceleration, arXiv:1510.01071. doi:10.48550/arXiv.1510.01071.
Russell, C.T., 2010. The Mars Plasma Environment. Springer Science & Business Media. https://doi.org/10.1007/978-0-387-70943-7.

Saharia, K., Goswami, K., 2007. One-dimensional Vlasov simulation of parallel electric fields in two-electron population plasma. Physics of Plasmas 14 (9), 092302. https://doi.org/10.1063/1.2770002.

Saharia, K., Goswami, K., 2008. Evolution of electron holes in two electron population plasmas. Physics of Plasmas 15 (12), 122311. https://doi.org/10.1063/1.3050065.

Schamel, H., 2023. Pattern formation in Vlasov–Poisson plasmas beyond Landau caused by the continuous spectra of electron and ion hole equilibria. Reviews of Modern Plasma Physics 7 (1), 11. https://doi.org/10.1007/s41614-022-00109-w.

Sharifi, M.A., Farzaneh, S., 2016. Local ionospheric modeling using the localized global ionospheric map and terrestrial gps. Acta Geophysica 64, 237–252. https://doi.org/10.1515/acgeo-2015-0065.

Sharma, G., Deka, K., Paul, R., et al., 2022. Experimental study on controlled production of two-electron temperature plasma. Plasma Sources Science and Technology 31 (2), 025013. https://doi.org/10.1088/1361-6595/ac4c4b.

Singh, N., Loo, S., Wells, B.E., et al., 2000. Three-dimensional structure of electron holes driven by an electron beam. Geophysical Research Letters 27 (16), 2469–2472. https://doi.org/10.1029/2000GL003766.

Singh, S., Reddy, R., Lakhina, G., 2009. Broadband electrostatic noise and low-frequency waves in the Earth's magnetosphere. Advances in Space Research 43 (12), 1940–1944. https://doi.org/10.1016/j.asr.2009.02.015.

Sun, H., Chen, J., Kaganovich, I.D., et al., 2022. Physical regimes of electrostatic wave-wave nonlinear interactions generated by an electron beam propagating in a background plasma. Physical Review E 106 (3), 035203. https://doi.org/10.1103/PhysRevE.106.035203.

Tokar, R.L., Gary, S.P., 1984. Electrostatic hiss and the beam driven electron acoustic instability in the dayside polar cusp. Geophysical Research Letters 11 (12), 1180–1183. https://doi.org/10.1029/GL011i012p01180.